A modeling study of Typhoon Nari (2001) at landfall: 2. Structural changes and terrain-induced asymmetries

Ming-Jen Yang,[1] Da-Lin Zhang,[2] Xiao-Dong Tang,[3] and Yi Zhang[3]

Received 5 December 2010; revised 17 February 2011; accepted 25 February 2011; published 13 May 2011.

[1] In this study, a series of model output diagnoses using the cloud-resolving simulations of Typhoon Nari (2001) with or without Taiwan topography is performed to gain insight into the landfall characteristics of the storm as it moves across Taiwan Island. Various kinematic and precipitation features prior to and after landfall are examined with a focus on the dynamic effects of Taiwan's high topography upon the generation of Nari's asymmetric structures. Results show that tangential winds weaken, whereas the low-level inflows and midlevel outflows increase, after landfall due to the increased friction and terrain blocking. Meanwhile, the eye wall updrafts exhibit more cellular structures and tend to tilt more outward with height over the high topography. However, Nari's primary and secondary circulations are stronger in the presence of terrain than those without terrain. The radii of the maximum winds and the eye wall updrafts could contract further after landfall, with more pronounced contraction occurring in the portion of the eye wall where more terrain retardation and blocking are present. In particular, the high topography allows the elevated low equivalent potential temperature (θ_e) air over the rugged terrain to intrude into the inner core region, causing the breakdown of the eye wall. It is concluded that the interaction of Nari's circulations with the elevated low-θ_e air, combined with topographical effects, accounts for most of the asymmetrical structures after landfall.

Citation: Yang, M.-J., D.-L. Zhang, X.-D. Tang, and Y. Zhang (2011), A modeling study of Typhoon Nari (2001) at landfall: 2. Structural changes and terrain-induced asymmetries, *J. Geophys. Res.*, *116*, D09112, doi:10.1029/2010JD015445.

1. Introduction

[2] Despite considerable tropical cyclone (TC) research, our understanding of their temporal and structural changes at landfall still remains limited, in part due to the lack of high-resolution observations during the life cycle of TCs. Earlier observational studies using in situ aircraft measurements and sounding data showed the basic three-dimensional (3-D) structures of TCs, such as the eye, the eye wall, and the circular high-wind zones [*Riehl*, 1948; *Simpson*, 1952; *Riehl*, 1954; *Stear*, 1965; *Shea and Gray*, 1973]. Recent studies with improved observing platforms examined the concentric eye wall structures [*Willoughby et al.*, 1982], the detailed organization and evolution of clouds and precipitation in the inner core regions [*Jorgensen*, 1984a, 1984b], and the axisymmetric versus asymmetric nature of TCs [*Marks and Houze*, 1987; *Marks et al.*, 1992; *Houze et al.*, 2006]. However, these observational studies were mainly of oceanic TCs, and only few of them analyzed their landfall characteristics.

[3] Similarly, numerous theoretical and modeling studies have investigated the structures and dynamics of TCs, such as the secondary circulations [*Willoughby*, 1979; *Schubert and Hack*, 1982; *Zhang et al.*, 2000], concentric eye wall and eye wall contraction [*Shapiro and Willoughby*, 1982; *Liu et al.*, 1999; *Zhu et al.*, 2004], spiral rainbands [*Willoughby*, 1979; *Guinn and Schubert*, 1993], and the eye dynamics [*Smith*, 1980; *Emanuel*, 1997; *Zhang and Kieu*, 2006]. In contrast, only a limited number of modeling studies have examined the landfall of TCs. *Tuleya* [1994] studied the impact of land surface conditions on landfall TCs. *Chen and Yau* [2003] examined the asymmetric structures of an idealized TC-like vortex after landfall. *Bender et al.* [1987], *Yeh and Elsberry* [1993a, 1993b], and *Lin et al.* [1999] explored track deflections as a TC approaches a mountainous island such as Taiwan. Orographic rainfall at TC landfall has also been previously examined [*Lin et al.*, 2002; *Wu et al.*, 2002; *Yang and Ching*, 2005; *Lee et al.*, 2008]. However, little is understood about the structural changes of precipitation and kinematics at landfall and their associated physical mechanisms, particularly in the presence of high topography.

[4] The objectives of the present study are (1) to investigate the structural changes of precipitation and kinematic fields prior to and after landfall and (2) to gain insight into the terrain-induced asymmetry in storm structures after landfall. These objectives will be achieved by diagnosing

[1]Department of Atmospheric Sciences, National Central University, Chung-Li, Taiwan.
[2]Department of Atmospheric and Oceanic Science, University of Maryland, College Park, Maryland, USA.
[3]Key Laboratory of Mesoscale Severe Weather of Ministry of Education, School of Atmospheric Sciences, Nanjing University, Nanjing, China.

0148-0227/11/2010JD015445

several 84 h quadruply nested (control and sensitivity) simulations of Typhoon Nari (2001) during its oceanic intensification, landfall, and passage over Taiwan's Central Mountain Range (CMR) with terrain peaks exceeding 3 km above sea level.

[5] *Yang et al.* [2008] (hereafter referred to as part 1) described the control and terrain-sensitivity simulations of Nari using the Pennsylvania State University–National Center for Atmospheric Research (PSU-NCAR) mesoscale model (i.e., MM5) with the finest grid resolution of 2 km. They showed that the model reproduces reasonably well the storm track, sizes and contraction of the eye and eye wall, the rapid pressure rise (~1.67 hPa h^{-1}) during landfall, as well as the rainfall distribution and local rainfall maxima associated with the Taiwan orography. Thus, these simulations provide a four-dimensional, dynamically consistent model data set to aid in the understanding of the storm's landfall characteristics and the terrain-induced asymmetric structures.

[6] Section 2 describes the model background and analysis procedures. Section 3 examines the structures of the precipitation and kinematics fields from the control, terrain-sensitivity and ocean experiments. The orographic impact on Nari's primary and secondary circulations, and the storm contraction during landfall are presented in section 4. The breakdown of Nari's eye wall after landfall is shown in section 5. Concluding remarks are given in section 6.

2. Model Description and Analysis Procedures

[7] In this study, the 84 h (1200 UTC 15 September to 0000 UTC 19 September 2001) simulations from the control run, terrain-sensitivity experiments, and the ocean run on the finest 2 km grid in part 1 are used. The 2 km grid simulations were performed on the grid of (x, y, σ) dimensions of 271 × 301 × 32 covering a horizontal area of 540 km × 600 km. The initial and lateral boundary conditions were provided from the outputs of the 6 km grid, which was obtained by first running the triply nested domains (54, 18, and 6 km) separately. The 2 km cloud-resolving simulations use three-ice microphysics scheme [*Reisner et al.*, 1998] including the mixing ratios of water vapor (q_v), cloud water (q_c), cloud ice (q_i), rainwater (q_r), snow (q_s), and graupel (q_g). The terrain-sensitivity experiments are conducted by reducing the height of Taiwan topography to 50% and 0%, respectively; the ocean run is conducted by replacing the land use data on Taiwan with ocean surface conditions. See Part 1 for the detailed model descriptions. Note that in Part 1, we have shown the effects of Taiwan topography on the track, intensity, and surface precipitation during the landfall of Nari, but not the corresponding 3-D structural changes.

[8] Because of the dominant axisymmetric nature of Nari's primary circulation, it is more convenient to examine its symmetric structures by transforming all MM5 prognostic variables from the (x, y, σ) coordinates into the cylindrical (r, θ, z) coordinates. The origin of the cylindrical coordinates is defined at the storm center, which is located at the minimum surface central pressure while Nari is over ocean but at the vortex circulation center above terrain peaks while it is over land. The axisymmetric component of any meteorological variable is obtained following the procedures of *Marks et al.* [1992], *Roux and Viltard* [1995], and *Liu et al.* [1999].

[9] Three stages of Nari's development are chosen for the present study: an oceanic stage (i.e., with little land influences), a partial landfall stage (i.e., with half of Nari's vortex circulation over Taiwan island), and a full landfall stage (i.e., with Nari's circulation fully over Taiwan island). The three stages are at 8 h prior to (t = 14 h), 2 h (t = 24 h), and 8 h after landfall (t = 30 h), respectively. Some fields are horizontally or vertically slice-averaged to display representative structures after minimizing small-scale fluctuations.

3. Topographic Effects on Landfall Structures

[10] To provide an appropriate framework for the subsequent discussion of Nari's structural changes, the middle level mean (σ = 0.4–0.8) radar reflectivity fields and low-level mean (σ = 0.7–1) horizontal wind vectors of Nari prior to and at the time of landfall are shown in Figures 1a and 1b, respectively. Nari's precipitation structures over the ocean are more or less circular, especially for a cloud-free eye and eye wall, as well as nearly symmetric spiral rainbands (Figure 1a). In contrast, the eye size decreases as the storm makes landfall on the northeastern Taiwan, and the cloud-free eye diminishes shortly after (Figure 1b). While precipitation is enhanced on the northwestern coast (i.e., the windward side), it is suppressed on the northeastern Taiwan (i.e., the lee side). Taiwan topography appears to account for the generation of more rainfall along the mountain ridges in the southwest quadrant as the moist tangential flow is lifted, and less rainfall is found in the southeast quadrant (Figure 1b).

[11] Nari's azimuthally averaged radar reflectivity and secondary circulations 8 h prior to landfall show the typical vertical structures of a mature oceanic TC, such as strong updrafts located slightly inside intense radar echoes in the eye wall, and weaker and more horizontally uniform echoes in outer rainbands (Figure 2a). These simulated vertical structures are similar in many aspects to those shown by *Marks and Houze* [1987, Figure 3], *Liu et al.* [1999, Figure 3], and *Braun* [2006, Figure 5]. Specifically, deep updrafts of greater than 2.7 m s^{-1} appear at z = 6 km in the eye wall, while downdrafts of 0.3 m s^{-1} occur at the interface between the eye and eye wall (Figure 2b). In addition, weaker but broader mesoscale updrafts are simulated at the middle to upper levels (z = 5–10 km) in outer rainbands, as shown in previous observational analysis [see *Marks and Houze*, 1987, Figure 6]. Higher equivalent potential temperature (θ_e > 372 K) air appears in the eye boundary layer, and the lowest-θ_e (<344 K) air occurs near z = 4 km in the outer region (r > 120 km) (Figure 2b). The maximum tangential wind is 59 m s^{-1} near the top of the marine boundary layer (MBL, i.e., z = 1 km), with its radius of maximum wind (RMW) vertically tilted outward (Figure 2c). Over the ocean, the simulated Nari has a hollow potential vorticity (PV) tower, similar to that shown by *Yau et al.* [2004], with the peak value of about 100 PVU (1 PVU = 10^{-6} m^2 s^{-1} K kg^{-1}) in the layer near z = 5 km (Figure 2c). Intense radial inflow (with a maximum value of 16 m s^{-1}) occurs in the lowest 1 km layer, with a shallow and weak inflow near the melting level (z = 5 km). The maximum outflow of 7 m s^{-1} occurs in a deep layer above (i.e., z = 6–15 km) in the eye wall (Figures 2a and 2d).

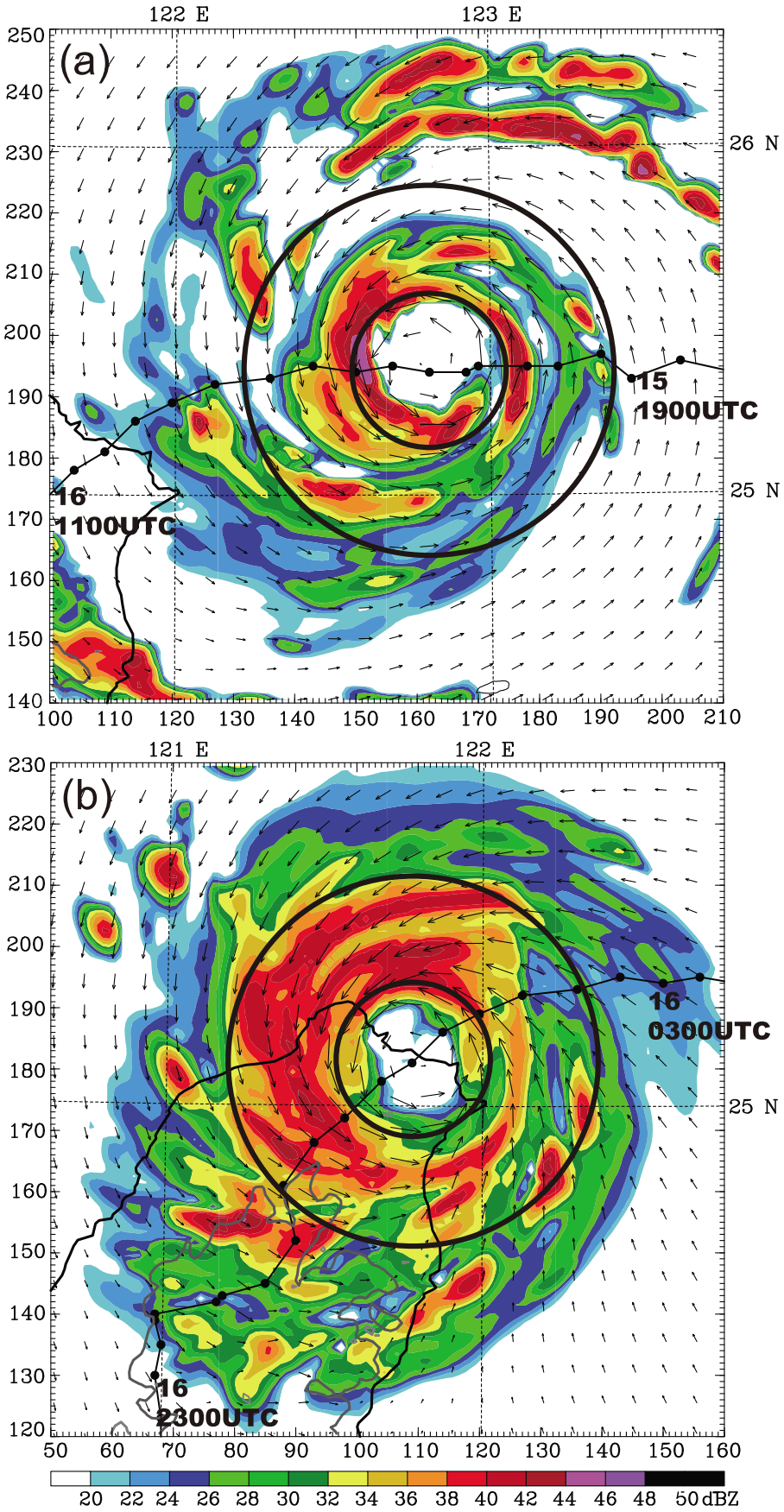
(a)
122 E
123 E
26 N
25 N
15
1900UTC
16
1100UTC
(b)
121 E
122 E
25 N
16
0300UTC
16
2300UTC
20 22 24 26 28 30 32 34 36 38 40 42 44 46 48 50 dBZ

Figure 1

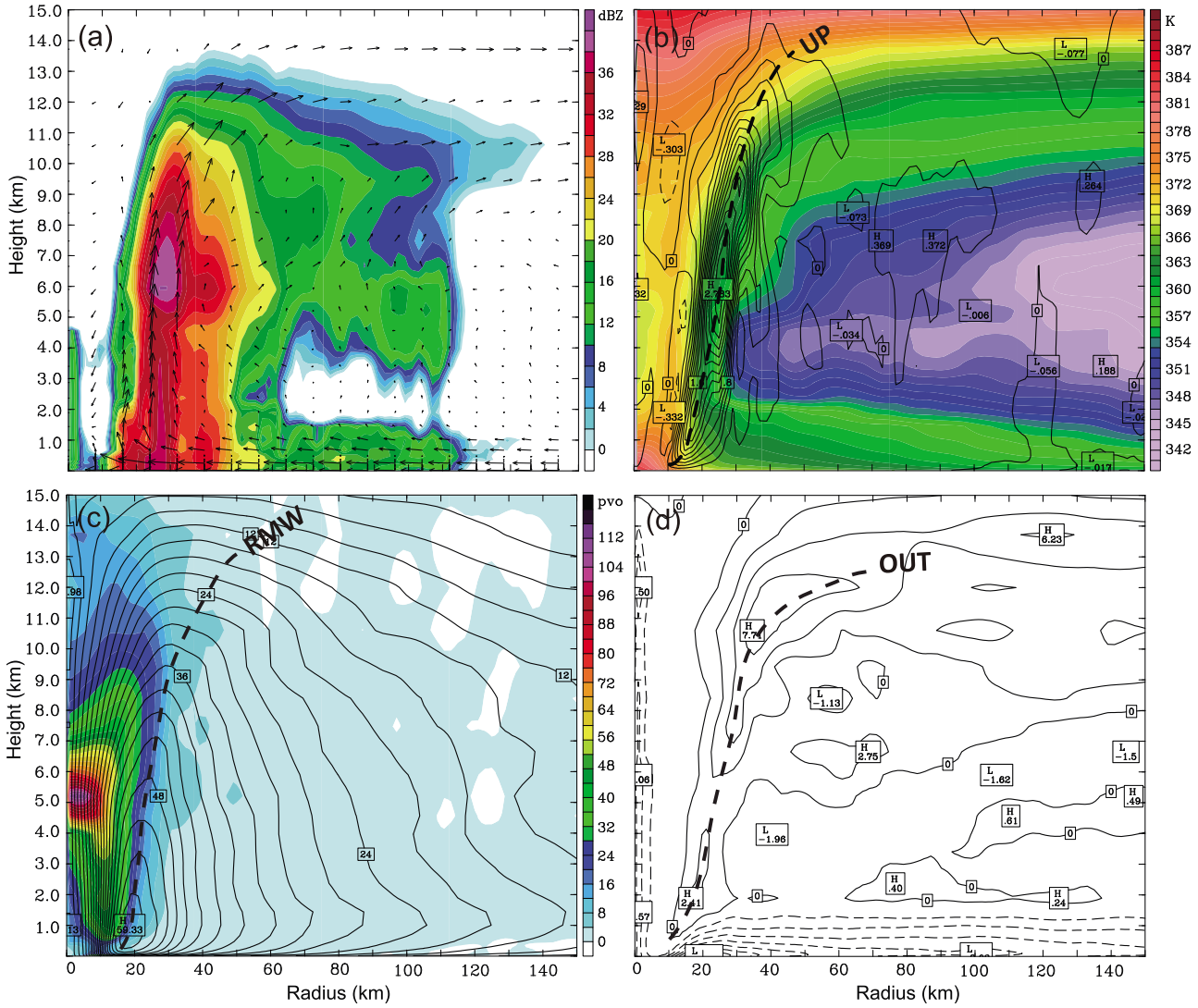

Figure 2. Vertical cross sections of the azimuthally averaged (a) radar reflectivity (in dBZ; colored), (b) vertical velocity (in m s^{-1}; contoured) and equivalent potential temperature (in K; colored), (c) tangential velocity (in m s^{-1}; contoured) and potential vorticity (in PVU; 1 PVU = 10^{-6} m^2 s^{-1} K kg^{-1}; colored), and (d) radial wind (in m s^{-1}) at 14 h (0200 UTC 16 September 2001). Contour intervals are 0.2 m s^{-1} in Figure 2b, 3 m s^{-1} in Figure 2c, and 2 m s^{-1} in Figure 2d, respectively. The radius of maximum wind and the axes of the eye wall updrafts and the axes of the outflows are represented by RMW, UP, and OUT, respectively.

[12] Part I has shown the significant influence of the CMR on the distribution of Nari's surface precipitation, namely, with the heaviest rainfall occurring on the upstream side. Part I has further shown that Nari generates much less surface rainfall than that in the control run when the CMR elevation is substantially reduced, due partly to the reduced topographical lifting and partly to the changing tracks (see Figure 20 and Tables 5 and 6 in part 1). These terrain-sensitivity and ocean simulations are diagnosed herein to see how their corresponding structural differences of 3-D precipitation and kinematic fields are generated. For this purpose, Figures 3a–3c compares the midlevel mean radar reflectivities from different simulations at the landfall time. Note that the landfall time is defined as the time when the simulated storm center is near the coastline, which is t = 22 h, 21 h, and 20 h for the full-terrain, the no-terrain, and the ocean runs, respectively. The difference in timing indicates that the CMR's blocking and land frictional effects tend to slow down Nari's movement by a couple of hours close to

Figure 1. Midlevel mean (σ = 0.4–0.8) radar reflectivity (dBZ, colored) and low-level mean (σ = 0.7–1) horizontal wind vectors from the 2 km grid at (a) 0200 UTC (t = 14 h) and (b) 1000 UTC (t = 22 h) 16 September 2001, superposed with the 1000 m terrain height (in thick gray line). Thick solid lines show horizontal rings of R = 25 km and R = 60 km, and the simulated track is indicated at hourly intervals.

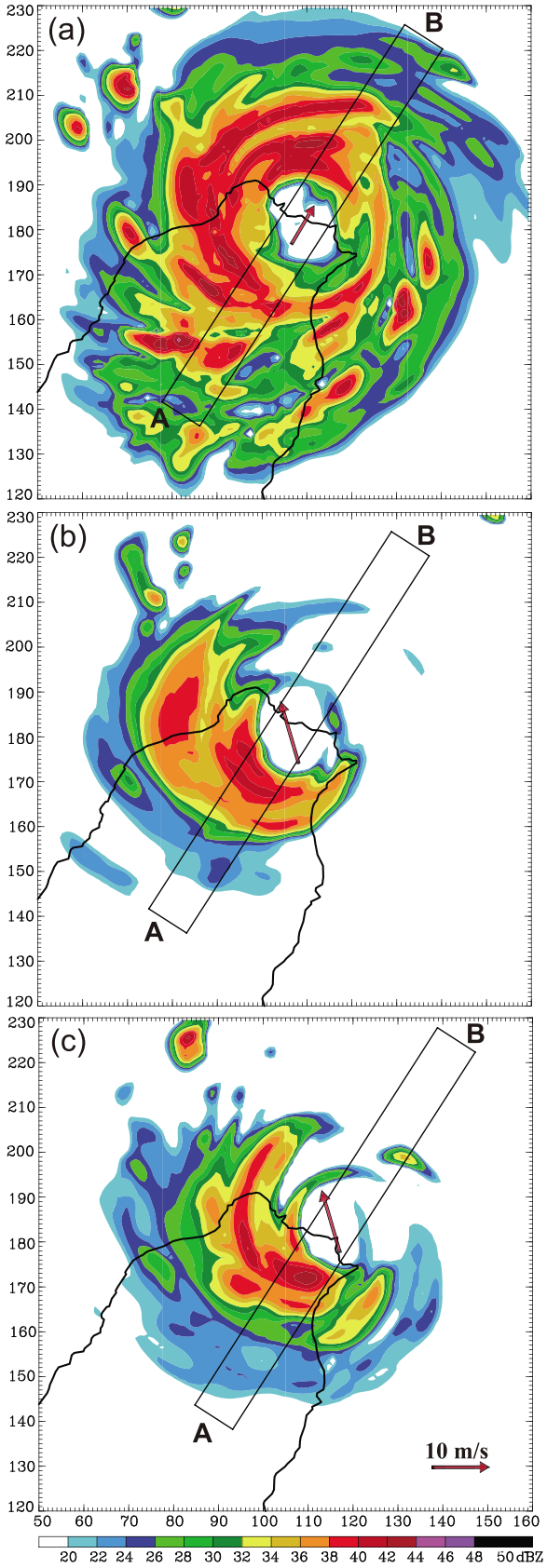

landfall, which is consistent with the previous idealized simulation studies [*Tuleya*, 1994; *Lin et al.*, 1999].

[13] It is obvious from Figure 3 that the eye size is somewhat smaller and precipitation is more widespread in the eye wall and spiral rainbands in the 100% terrain experiment, compared to the no-terrain and ocean runs. In addition, locally stronger (weaker) echoes are simulated on the upstream (downstream) sides of the CMR, respectively, as expected by the strong topographical forcing. In contrast, the no-terrain experiment produces weaker and less widespread rainbands to the west and south (Figure 3b); similarly for the ocean run (Figure 3c). In the absence of the CMR, a wave number 1 rainfall pattern appears clearly in Figures 3b and 3c, namely, with most precipitation occurring in the southwest quadrant. This is in agreement with the downshear left generation of rainfall [*Black et al.*, 2002], given the environmental shear vector at the 200–850 hPa layer. In this regard, the topographically generated uplifting and downslope motion alter the shear-induced wave number 1 rainfall structures (compare Figures 3a, 3b, and 3c). The more widespread rainfall in the eye wall and outer rainbands in the full-terrain run can be attributed to the presence of stronger windward convergence of moisture and the cyclonic advection of convective cells that are generated on the upstream side of the CMR. The ocean run produces less rainfall in the eye wall at landfall, compared to the no-terrain run, indicating the favorable role of land frictional convergence in rainfall production in the presence of ample moisture (compare Figures 3b and 3c).

[14] Figure 4 shows vertical structures at landfall along the track passing through the major mountain peak (i.e., Mt. Snow) of the northern CMR. Robust eye wall updrafts with a deep layer of stronger radial inflow appear near the coast in the northeastern quadrant, despite the presence of favorable topographical lifting in the southwestern quadrant (Figure 4a). Furthermore, the eye wall updrafts over the northern CMR tilt more outward, which appears to be closely related to sloping radial outflows above the topography. Specifically, the sloping radial outflow of greater than 10 m s^{-1} over terrain (x = −60∼−10 km in Figure 4a) plays an important role in transporting hydrometeors outward from the inner core region and widening the rainfall area over the terrain (see Figures 1b and 3a). This process appears to be responsible for the generation of evaporatively driven downdrafts over the CMR (x = −80∼−50 km in Figure 4a). The blocking and surface frictional effects decrease the peak tangential wind from 65 m s^{-1} over the ocean portion to 60 m s^{-1} in the land portion of the eye wall.

[15] By comparison, removing the terrain heights produces very different secondary circulation structures from

Figure 3. The midlevel mean (σ = 0.4–0.8) radar reflectivity of (a) full-terrain, (b) no-terrain, and (c) ocean experiments at the time of landfall (t = 22 h, 21 h, and 20 h, respectively). The rectangle zone (with 200 and 20 km in the along-track and cross-track directions, respectively) used to perform the averaged vertical cross sections in Figures 4 and 5 is indicated. Arrow is the environmental shear vector between 200 and 850 hPa within 200 km from the typhoon center.

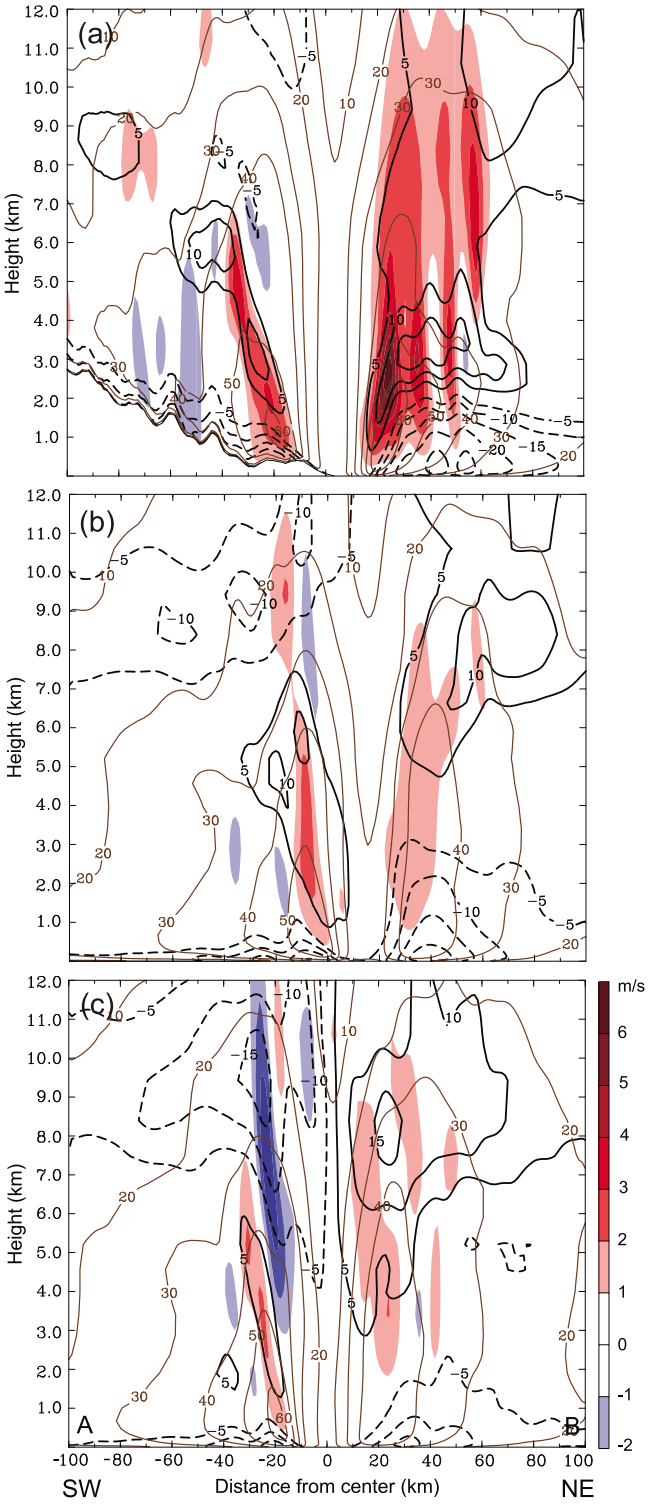

Figure 4. Vertical AB cross sections for the storm-relative tangential flow (brown, contoured at 10 m s^{-1}), radial flow (black, contoured at 5 m s^{-1}), and vertical velocity (colored) of (a) full-terrain, (b) no-terrain, and (c) ocean experiments averaged in the along-track (SW-NE) direction at time of landfall (t = 22 h, 21 h, and 20 h, respectively). Contours for zero radial flow are omitted. Horizontal areas used to take the averaged cross sections are shown by the rectangle zones in Figure 3.

those in the full-terrain run. That is, more robust updrafts and radial outflows are found in the southwestern eye wall (downshear left side) over land for the no-terrain experiment, as dictated by the environmental shear vector (Figure 4b). Similarly, stronger tangential winds with sharper reduction in the MBL, and a shallower layer of the low-level radial inflows appear over land than those over ocean (Figure 4b). These differences are more evident when the frictional effects are reduced in the ocean run (Figure 4c). Of significance is that despite the significant differences in the secondary circulation, relatively minor influences are present in tangential winds among the three experiments.

[16] The along-track vertical cross sections of equivalent potential temperature (θ_e) from the three experiments, given in Figure 5, show that with the Taiwan topography, the cyclonic downslope transport of midlevel low-θ_e air into lower levels tends to destroy the high-θ_e air within the boundary layer above terrain (left portion of Figure 5a). The secondary circulation within the eye wall near the coast is very pronounced with an upright orientation, due to the enhanced deep convection near the coast (Figures 4a and 5a). The eye wall over terrain is outward tilted with more slantwise secondary circulation (Figure 5a). In contrast, intense precipitation with deep radar echoes mainly occurs on the southwest quadrant and weak precipitation with shallow echoes appear on the northeast quadrant for the no-terrain and ocean runs (Figures 5b and 5c). The vertical θ_e structure and secondary circulation of the no-terrain run are very similar to those of the ocean run, except that the θ_e within the eye MBL air of the ocean experiment is higher than that of the no-terrain experiment by 2–3 K as a result of abundant moisture over ocean (Figures 5b and 5c).

[17] After seeing the topographical influences on Nari's primary and secondary circulations, it is of interest to examine the azimuthal distributions of precipitation and kinematic structures at landfall as imposed by the CMR at two different radii: R = 25 km and R = 60 km which are located in the eye wall and the outer rainband, respectively (see Figure 1b). At R = 25 km, right above the lowest 2 km layer of radial inflows is a shallow layer of an outflow jet circling the eye wall (Figure 6a). Deep updrafts occur above the CMR, with stronger upward (downward) motion on the upwind (lee) side and a deeper (shallower) bottom inflow layer (Figures 6a and 6b). The deep inflow layer on the upstream side is consistent with the more topographical lifting and intense rainfall. Note that the radially tilted secondary circulations could not be completely shown from such an azimuthal cross section. So, the radial inflows above z = 6 km over land coincides roughly with downdrafts at the eye–eye wall interface.

[18] Because of the spiral nature of the outer rainband, there are pronounced azimuthal variations in the secondary circulations at R = 60 km. Specifically, there are stronger radial inflows over the eastern (ocean) semicircle due to the presence of landward convergence, and more pronounced upper level outflows in the northern semicircle where a spiral rainband is present (compare Figures 6c and 1b). Localized convective cells (colored in yellow to orange) and moist downdrafts (dash contoured) exist in the outer rainband (Figure 6d). The local topography appears to account for some mountain wave-like features in vertical motion and scattered rainbands on the lee side in the south (compare

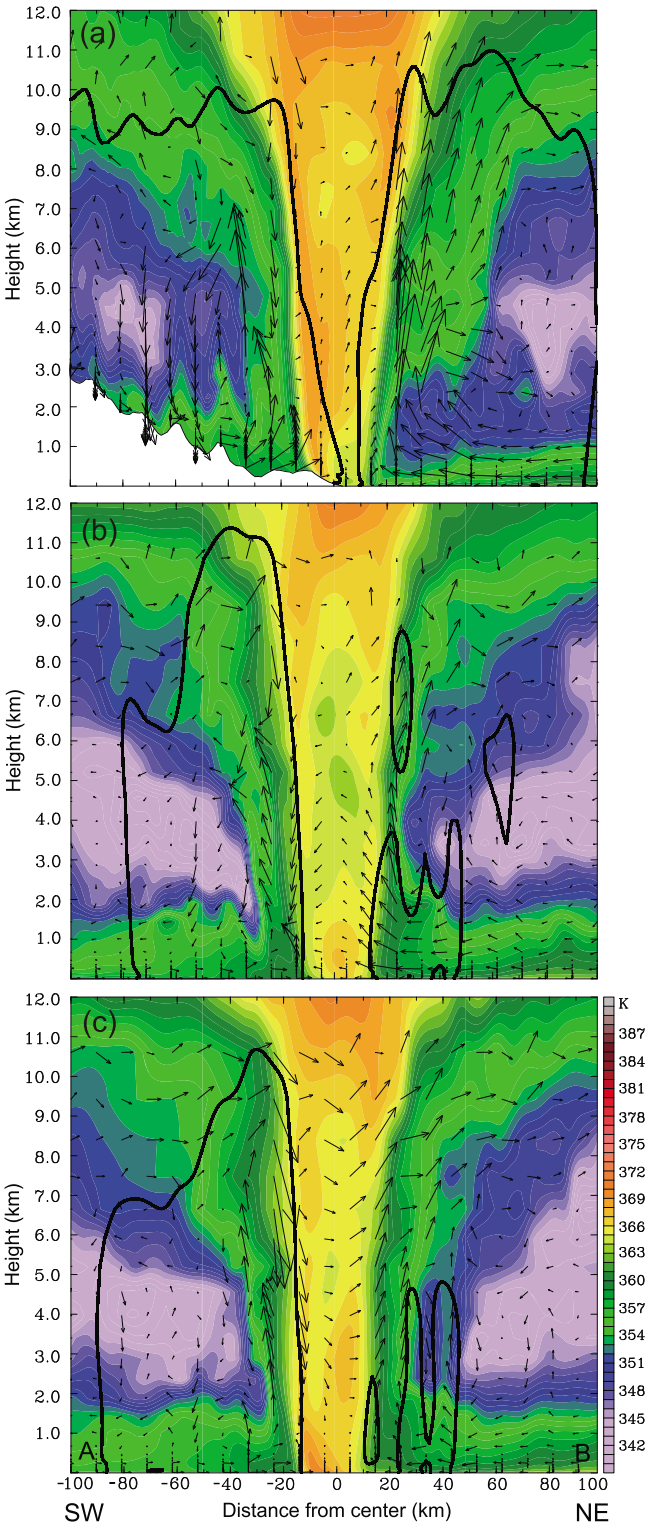

Figure 5. Same as Figure 4 but for the equivalent potential temperature, superimposed with storm-relative in-plane flow vectors of (a) full-terrain, (b) no-terrain, and (c) ocean experiments averaged in the along-track (SW-NE) direction at time of landfall (t = 22 h, 21 h, and 20 h, respectively). Bold outline is the 20 dBZ radar reflectivity contour.

Figures 6d and 3a). However, most of these features are absent when the CMR is removed (not shown). It follows that the presence of the CMR allows the generation of more organized convection in the eye wall (Figure 3a), more localized precipitation (see Figure 20 in part 1), and a more intense storm (i.e., heavier rainfall) at time of landfall (see Figure 17 in part 1) than those in the absence of the CMR.

[19] Figure 7 shows the time evolution of the vertical motion, horizontal divergence, and equivalent potential temperature (θ_e) within an area of 12 km × 12 km centered at the eye during Nari's 18 h landfall period (t = 18–36 h). When Nari is over the ocean (i.e., t = 18–21 h), its eye has the typical vertical structures of weak subsidence above (i.e., in the layer of σ = 0.8–0.2), and weak upward motion in the MBL (σ = 1–0.9). This weak MBL upward motion is consistent with the significant convergence associated with the Ekman pumping as shown by *Zhang and Kieu* [2006]. Upward motion begins to appear at the middle levels (σ = 0.8–0.4) 2 h prior to landfall (t = 20–22 h), and it extends to lower levels (σ = 0.95) after Nari's landfall (t = 24–27 h). Such a significant upward motion is attributed to the enhanced surface friction and topographical lifting, as indicated by the upward extension of the low-level convergence. Note the marked reduction of the surface θ_e values immediately after landfall over the eye, due to the absence of moisture flux over land and the subsequent intrusion of environmental lower-θ_e air. The strong upward motion accounts for the upward transport of the lower-θ_e (<356 K) air into the deep troposphere in Nari's central region. Pronounced downdrafts and divergence appear in the "eye" after landfall (e.g., t = 28–30 h), mainly due to the terrain effects (the center is located near the peak of Mt. Snow during this period; see Figures 1b).

4. Vortex Contraction After Landfall

[20] Previous observational and modeling studies have documented contraction of the eye wall as a phenomenon of TC growth over the ocean [*Willoughby et al.*, 1982; *Willoughby and Black*, 1996; *Liu et al.*, 1999]. One may speculate that the eye wall size would increase because TCs typically weaken after landfall. However, Figure 8 indicates that the surface RMW begins to shrink 2 h prior to landfall, and it occurs more rapidly after landfall, namely, a decrease of 7–8 km in the RMW during the period of 20–25 h. Similar shrinkage can also be found in the radii of the peak surface radial inflow and the midlevel updraft in the eye wall.

[21] Figure 8 also shows that the azimuthally averaged surface radial inflow and midlevel updraft experience substantial increases in both magnitude and coverage immediately after landfall, whereas the corresponding surface tangential wind decreases as the storm advances more into the land. These results are expected from the tremendous latent heat release associated with heavy rainfall as a result of both the topographical lifting and Nari's slow movement. Both the surface radial inflow and the midlevel updraft are peaked about 10 km radially outward from the RMW, which are similar to those shown for an oceanic TC [see *Liu et al.*, 1999, Figure 3]. About 4 h after landfall, the midlevel updraft core expands outward and weakens gradually, so does the azithimuthally averaged surface radial inflow.

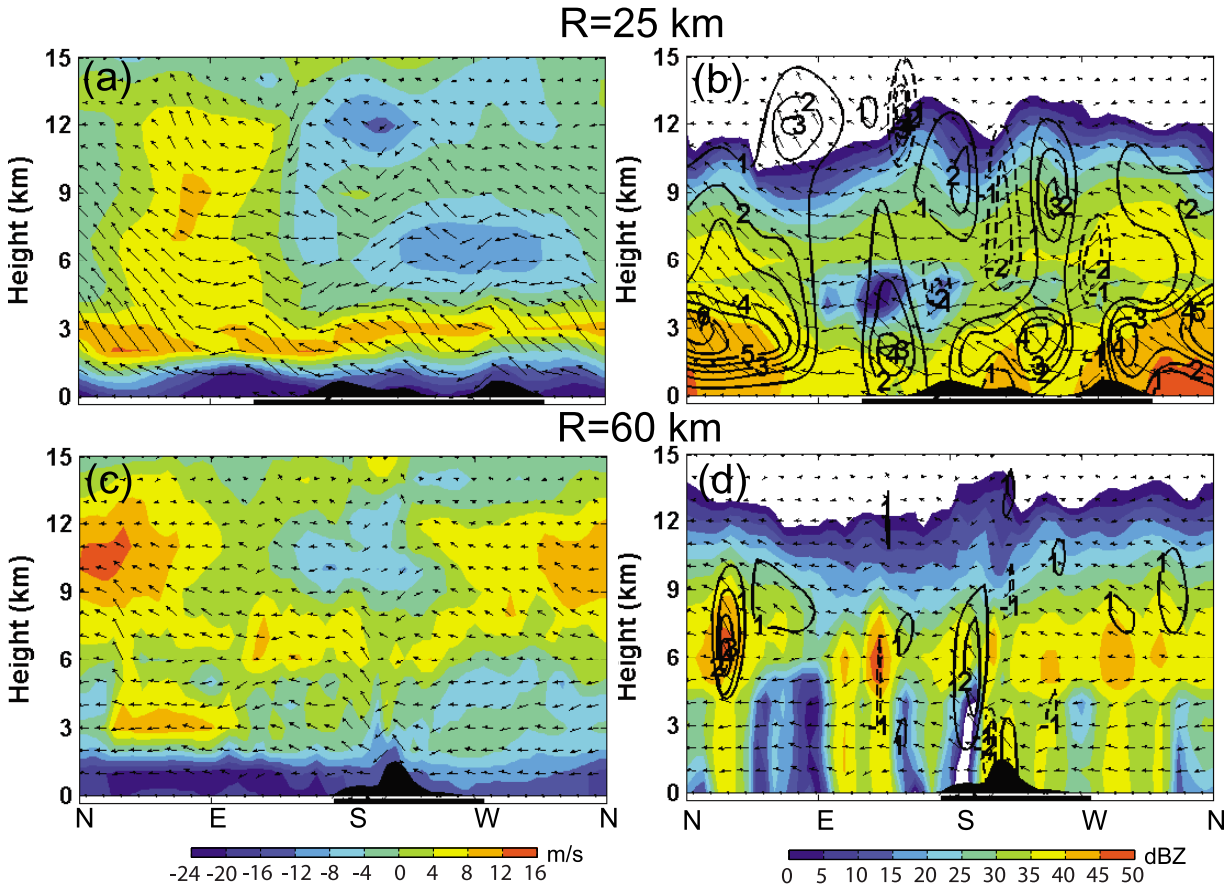

Figure 6. Azimuth-height cross sections of (a–c) the storm-relative radial winds (at intervals of 4 m s^{-1}) and in-plane flow vectors; (b–d) radar reflectivity (colored) and vertical velocity (at intervals of 1 m s^{-1}) taken along a circle with radii of 25 (Figures 6a and 6b) and 60 km (Figures 6c and 6d), respectively, from the simulation result at t = 22 h. The black bar indicates the land portion.

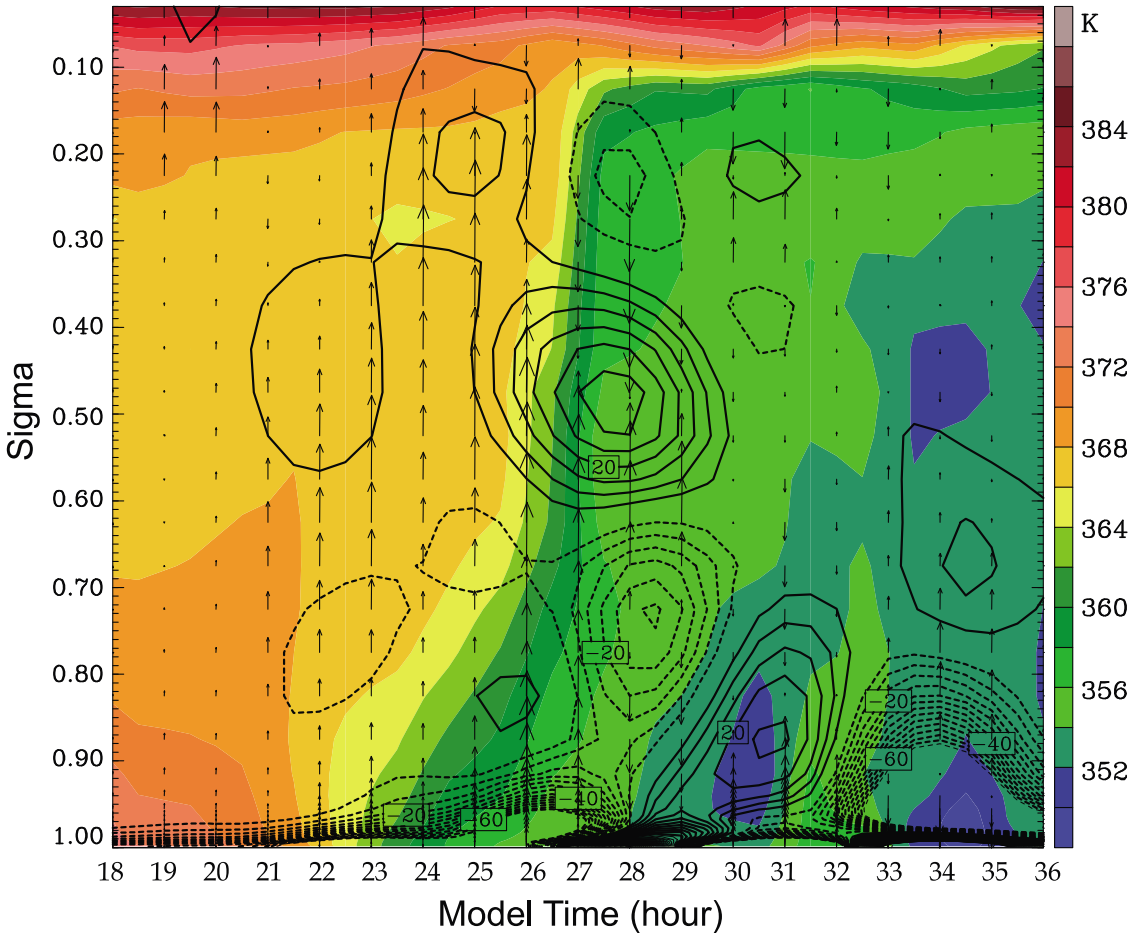

Figure 7. The time-height cross section of the equivalent potential temperature (K, colored), and horizontal wind divergence (every 10^{-3} s^{-1}; solid/dashed lines for divergence/convergence) averaged with an area of 12 km × 12 km centered in the eye. Vector is for vertical velocity. Note the landfall time at $t = 22$ h.

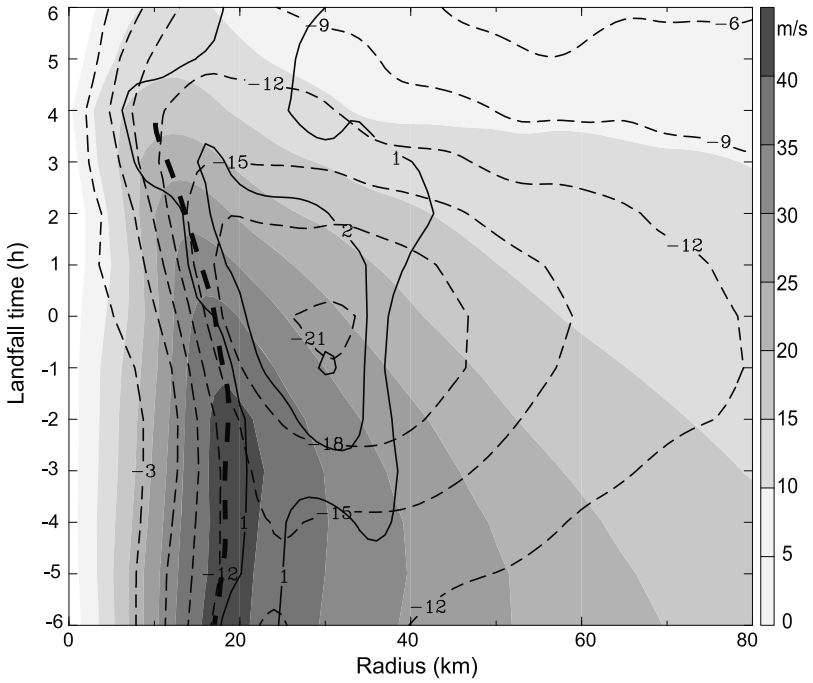

Figure 8. The time-radius cross section of azimuthally averaged fields of vertical velocity (W, solid line, contoured at 1 m s^{-1}) near 700 hPa (σ = 0.7), and storm-relative tangential (V'_t, shaded, m s^{-1}) and radial wind speeds (V'_r, dashed line, contoured at 3 m s^{-1}) near the surface (σ = 0.9985). The thick dashed line denotes the RMW near the surface.

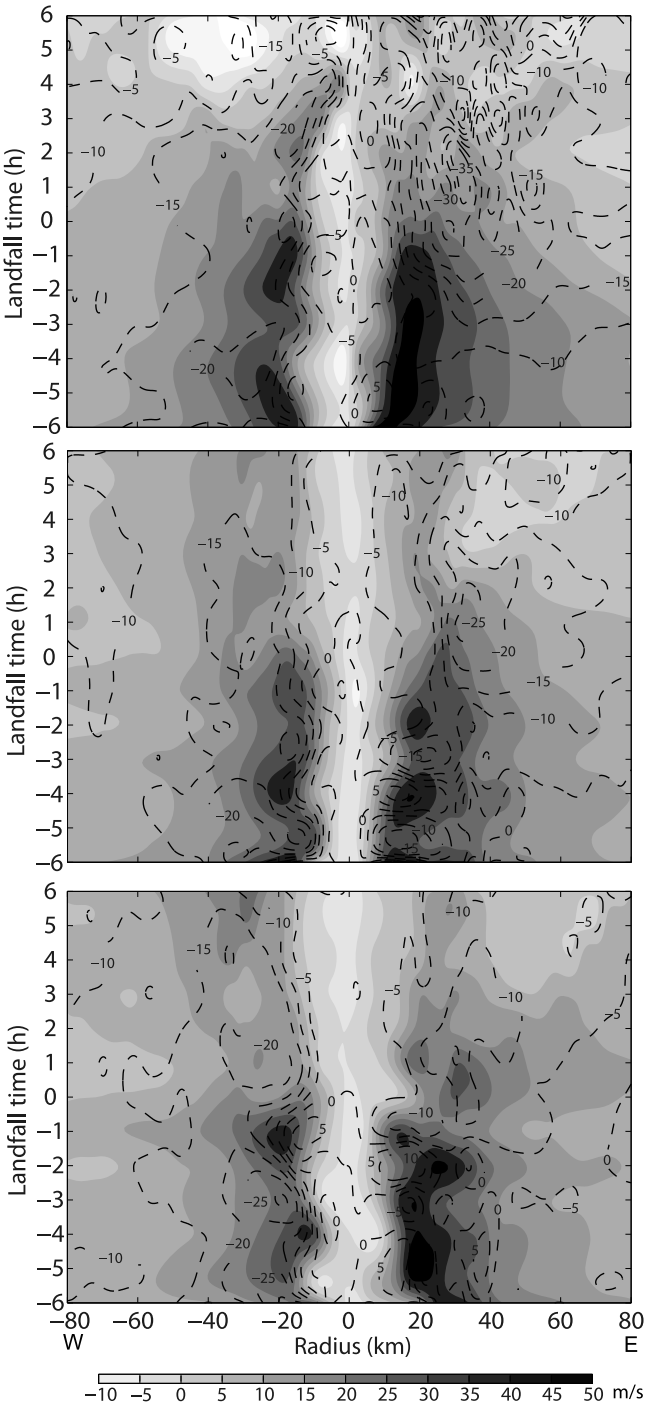

Figure 9. The time-radius cross section of near-surface (σ = 0.9985) storm-relative tangential wind (V'_t, m s^{-1}, shaded) and radial wind (V'_r, m s^{-1}, contoured at 10 m s^{-1}) in cross-track direction of (top) the full-terrain, (middle) 50%-terrain, and (bottom) no-terrain experiments. Minus (plus) landfall time denotes the time prior to (after) landfall.

[22] Since the western portion of Nari's circulation is subject to more retardation and blocking of the CMR compared to the eastern portion, we examine next whether the above mentioned eye wall contraction is indeed topographically forced. For this reason, Figure 9 compares the time diameter series of the surface tangential and radial winds across Nari's track 6 h prior to and after landfall between the full-, 50%-, and no-terrain experiments. Indeed, the RMW and radius of the peak radial inflow in the western eye wall of the full-terrain run shrink more significantly after landfall than those in the eastern eye wall, most of which are distributed offshore (Figure 1b). Of relevance is that the tangential wind in the western eye wall is even slightly greater than that in the eastern eye wall after Nari's center moves over land. However, the opposite is true for the surface radial inflow after landfall, i.e., with the peak intensity of −35 m s^{-1} offshore compared to only −15 m s^{-1} over the northern CMR. This indicates that the stronger radial inflows shown in Figures 6, 8, and 9 (top) are associated with the development of deep convection in the eye wall offshore.

[23] When the terrain heights are reduced by half, the above mentioned contraction does not become evident. But the surface radial inflow in the eastern eye wall is still stronger (peaked at −25 m s^{-1}) than that (peaked at −15 m s^{-1}) in the western eye wall (Figure 9, middle). When the CMR is completely removed, there is little evidence of the RMW shrinkage and little asymmetry can be seen from the surface tangential and radial flows (Figure 9, bottom). These results clearly demonstrate that the asymmetry of the secondary circulation and the contraction of the RMW during Nari's landfall are indeed caused by Taiwan's terrain, not by storm's internal dynamics.

5. The Eye Wall Breakdown After Landfall

[24] In this section, we examine the topographical impact on Nari's asymmetries after most of the vortex circulation moves into Taiwan Island. Thus, Figure 10 compares the cross-track vertical cross section of θ_e at t = 30 h, i.e., 8 h after landfall, from the control run to that in the no-terrain run. In the control run, this cross section is just taken through Mt. Snow, near which top Nari's eye is located (Figure 10a). Although the storm still exhibits the typical inward up–outward secondary circulation, we can see a well-developed eye wall on the windward (northwestern) side with a layer of higher-θ_e air ascending from the MBL into the upper layers, which is similar to that when Nari is over ocean (compare Figures 10a and 2b). In contrast, the eye wall structure on the lee (southeastern) side is obscured, where a deep layer of lower-θ_e air (barely ascending in the lowest layers) is flowing into the inner core region. Corresponding to the two different eye wall structures are intense updrafts on the windward side but weak upward motion on the lee side. Clearly, the high-θ_e air in the lee-side MBL could not be transported into this portion of the eye wall due to the weak upward motion, while the deep convergent inflows of lower-θ_e air above the MBL tend to induce moist downdrafts as it meets the cloudy air in the eye wall. Moreover, the elevated lower-θ_e air near the mountain surface is flowing cyclonically from the lee side and then across Mt. Snow to the other side, some of which intrudes into the eye region, leading to the breakdown of the eye wall (see trajectories D and F in Figure 13).

[25] By comparison, the storm displays a typical nondiluted eye with higher-θ_e air in the upper layers when Taiwan terrain is removed (Figure 10b). Note the presence of lower-θ_e air in the eye's boundary layer (compare Figures 10b and 2b),

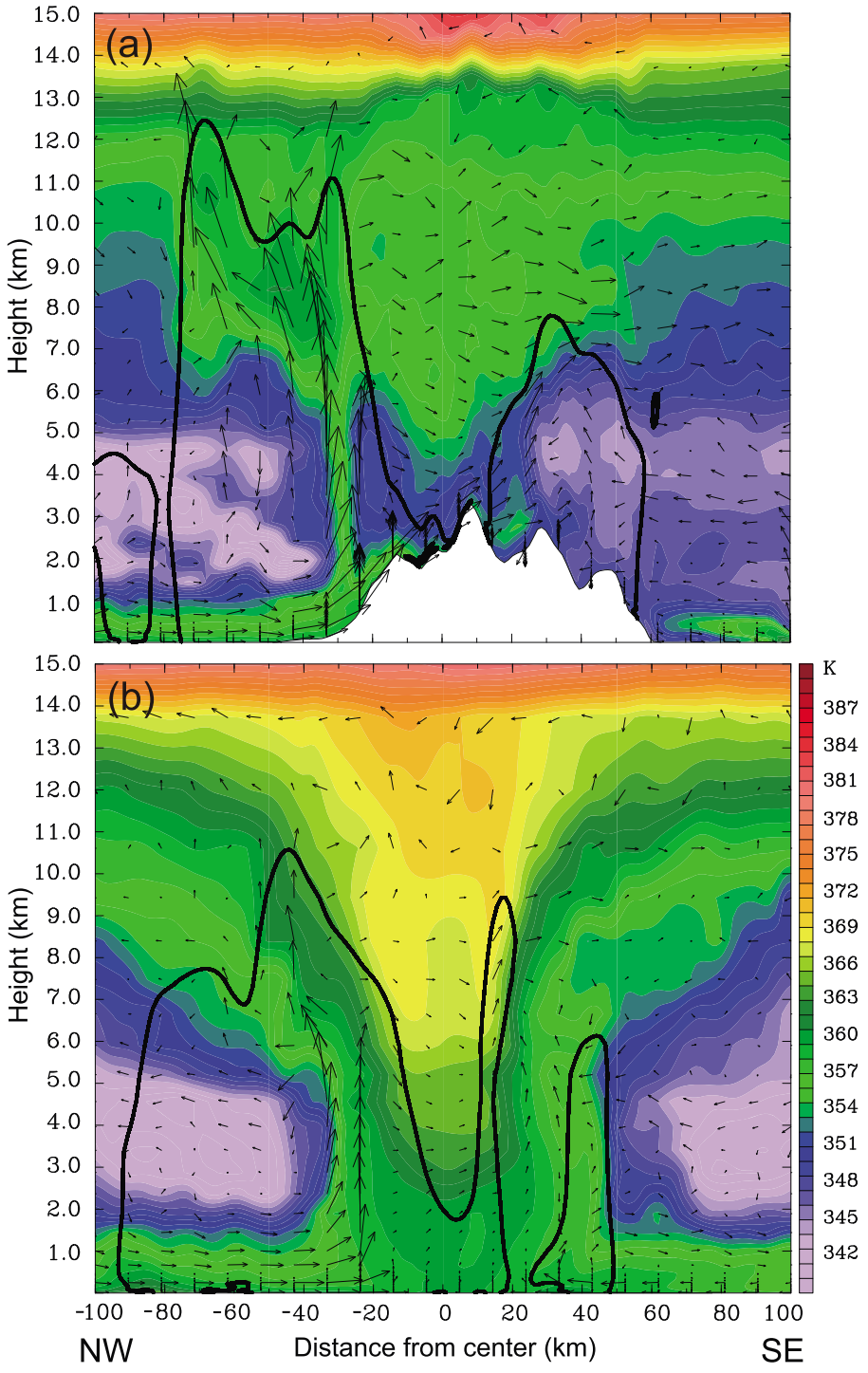

Figure 10. Vertical cross section of the across-track (seven-slice averaged; i.e., 12 km) equivalent potential temperature, superimposed with storm-relative in-plane flow vectors of (a) full-terrain and (b) no-terrain runs at t = 30 h (1800 UTC 16 September 2001). Bold outline is the 20 dBZ radar reflectivity contour. Horizontal position of the vertical cross section is shown in Figure 13a.

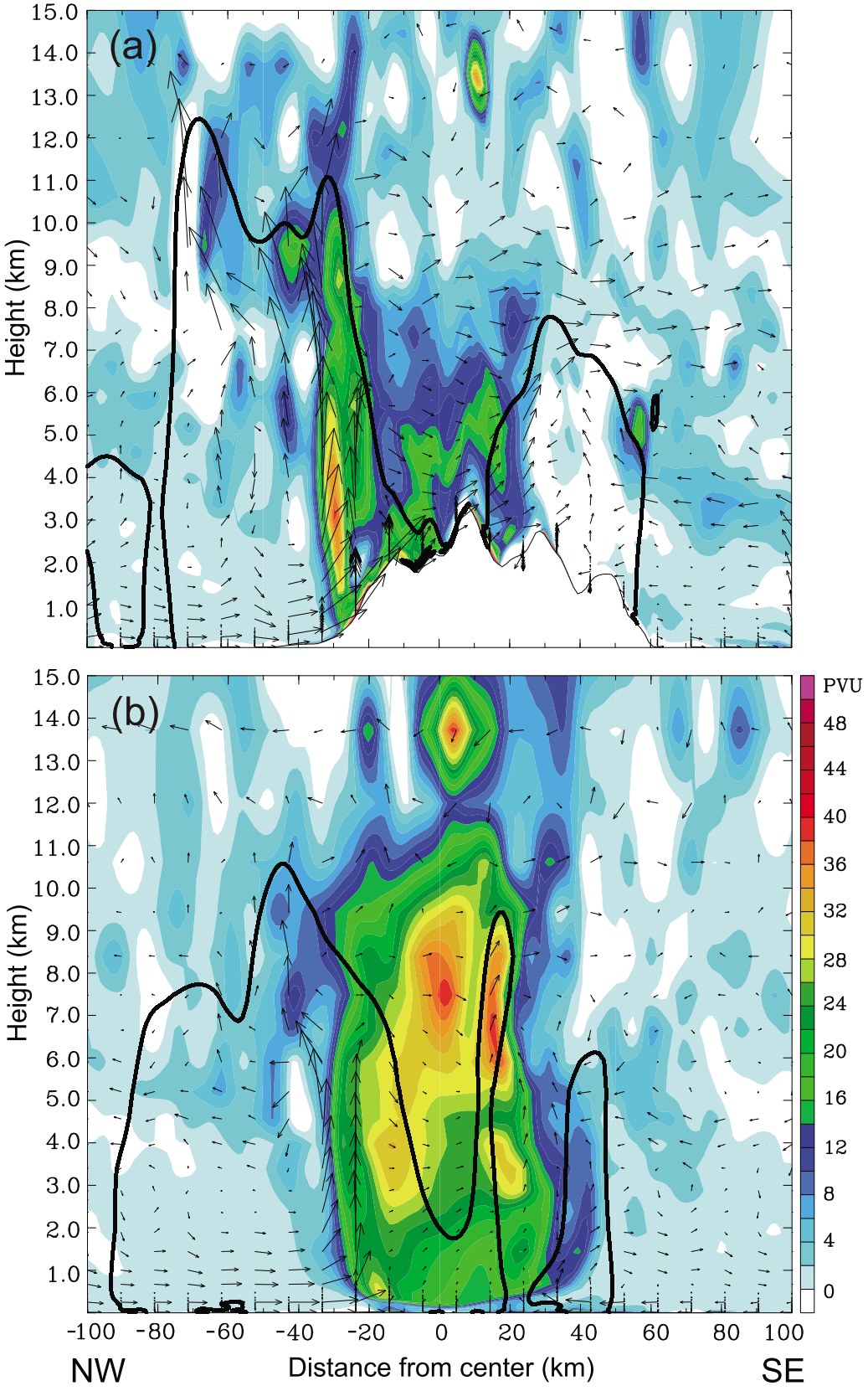

Figure 11. Same as Figure 10 but for the potential vorticity.

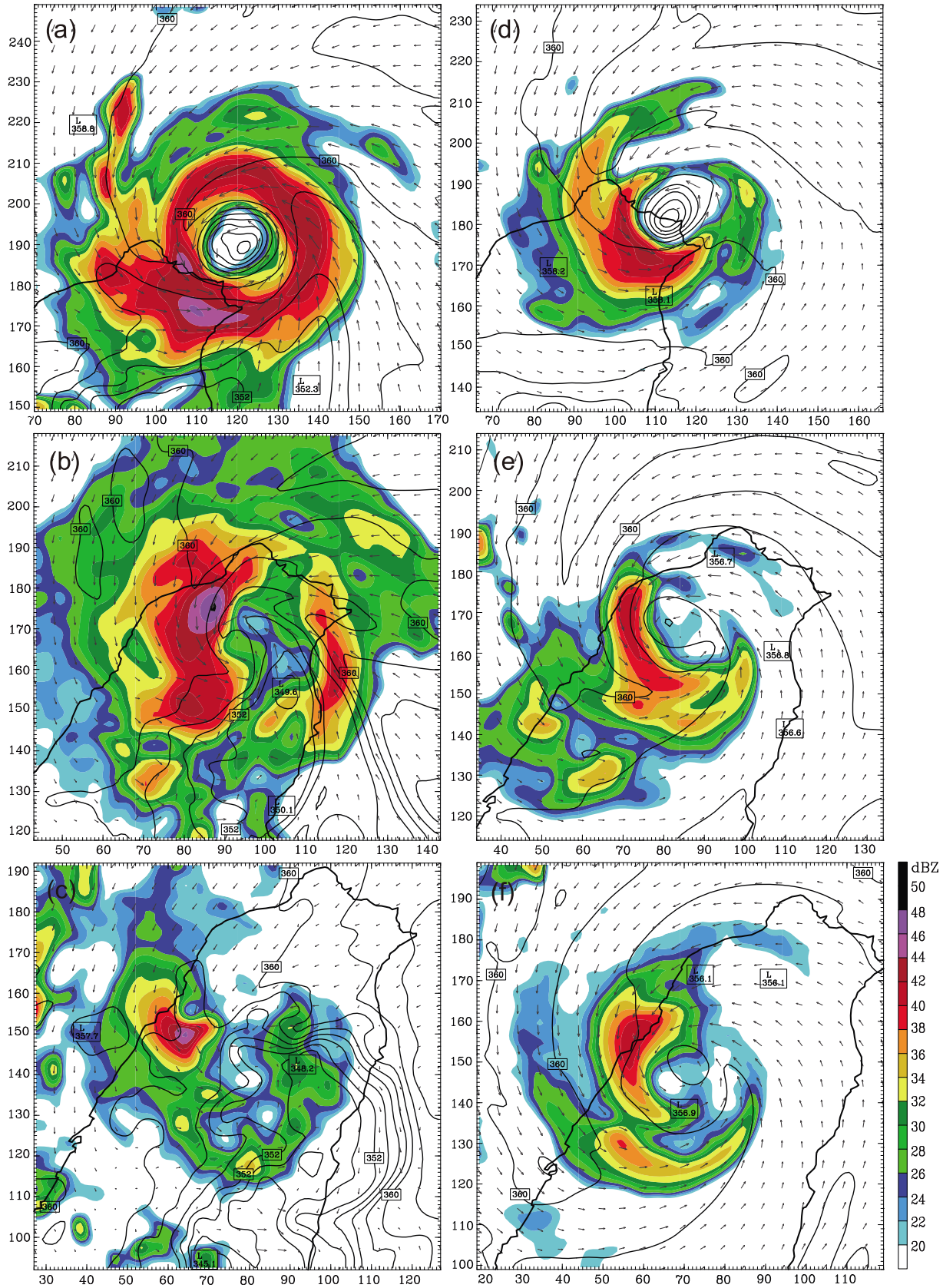

Figure 12. Horizontal distribution of the near-surface (σ = 0.996) equivalent potential temperature and radar reflectivity (colored, dBZ), superimposed with the surface flow vectors, from (a, d) t = 20 h, (b, e) t = 25 h, and (c, f) t = 30 h of full-terrain run (Figures 12a, 12b, and 12c) and no-terrain run (Figures 12d, 12e, and 12f).

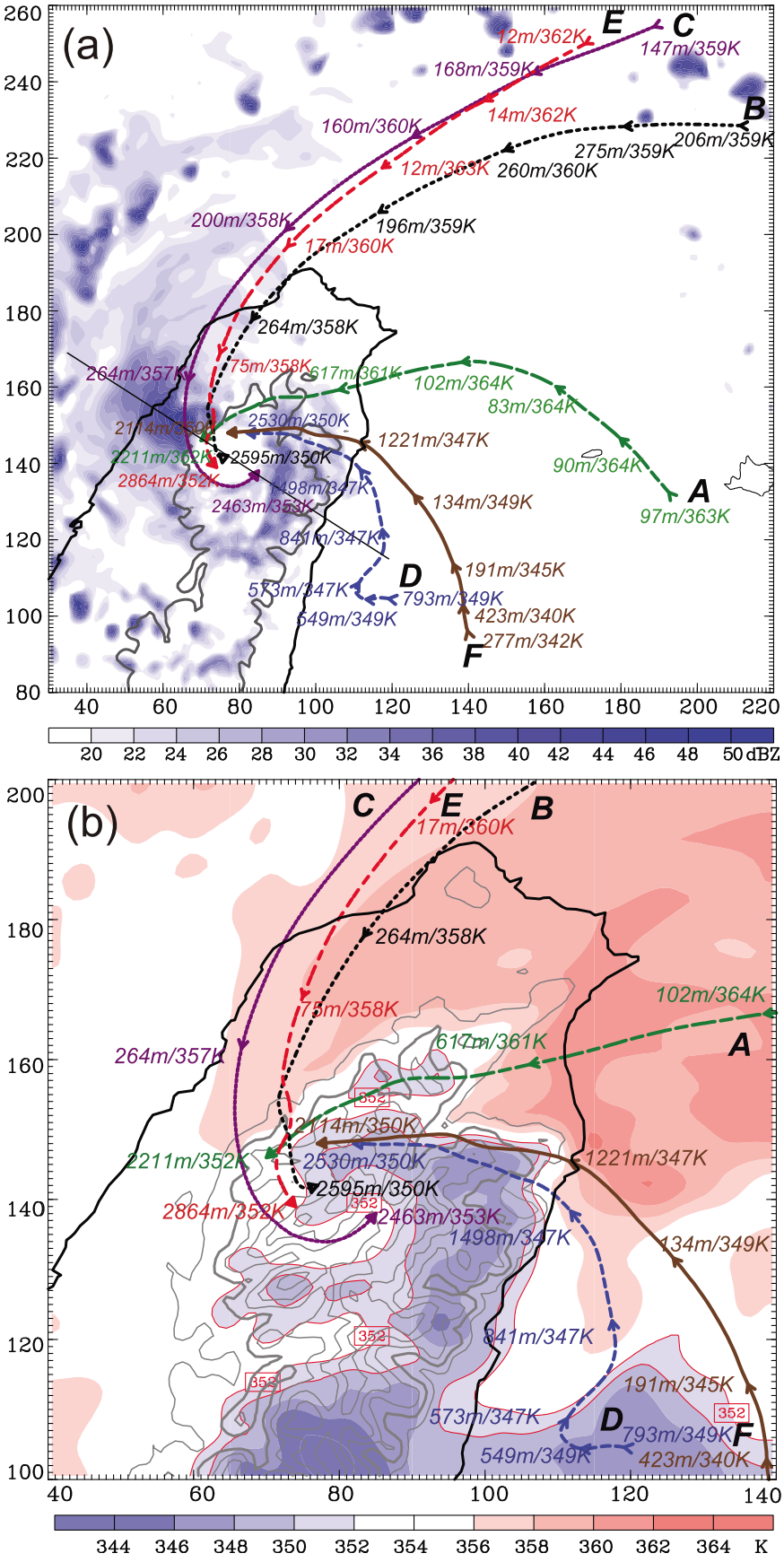
(a)
E
C
B
A
D
F
12m/362K
147m/359K
168m/359K
14m/362K
160m/360K
206m/359K
275m/359K
260m/360K
200m/358K
196m/359K
264m/358K
264m/357K
75m/358K
617m/361K
102m/364K
83m/364K
2530m/350K
1221m/347K
90m/364K
2595m/350K
2864m/352K
1498m/347K
134m/349K
2463m/353K
97m/363K
841m/347K
191m/345K
573m/347K
793m/349K
549m/349K
423m/340K
277m/342K
20 22 24 26 28 30 32 34 36 38 40 42 44 46 48 50 dBZ
(b)
C
E
B
17m/360K
264m/358K
75m/358K
102m/364K
264m/357K
617m/361K
A
352
2114m/350K
2211m/352K
2530m/350K
1221m/347K
2595m/350K
2864m/352K
2463m/353K
1498m/347K
134m/349K
841m/347K
191m/345K
573m/347K
D
793m/349K
F
549m/349K
423m/340K
344 346 348 350 352 354 356 358 360 362 364 K

Figure 13

which is of typical feature after landfall as a result of little surface moisture flux. Although the vertical motion field still shows the wave number 1 feature (also see Figure 3b), the higher-θ_e eye air and the lower-θ_e environmental air are clearly separated, like that when Nari is over ocean (compare Figures 10b and 2b), even in the presence of elevated radial inflows on the southeast side. A comparison between Figures 10a and 10b reveals not only organized strong lifting and deep updrafts in the eye wall on the windward side, but also continuous ascending in the "remnant eye wall" on the lee side, albeit with weak intensity.

[26] Figure 11a shows the asymmetry or breakdown of the eye wall in the full-terrain run from the PV perspective. The highest PV of about 40–50 PVU, which is much smaller than that shown in Figure 2c, is concentrated in the northwestern eye wall. Like the θ_e structure, PV decreases monotonically outward from the TC center on the lee (southeastern) side. When Taiwan terrain is removed, PV of greater than 40 PVU remains in the upper portion of the eye wall (Figure 11b). Comparing Figures 11a and 11b further confirms the breakdown of the eye wall in the presence of the high topography. Thus, we may state that the eye wall breakdown is caused by the interaction of the TC vortex circulation with the asymmetric topographical forcing, irregular terrain-induced disturbances, and different thermodynamic properties between the MBL and an elevated boundary layer.

[27] To help understand the above mentioned topographical impact, Figure 12 compares the evolution of Nari's surface circulation interacting with the near-surface θ_e and radar reflectivity during a 10 h landfall period in the full-terrain experiment to that in the no-terrain experiment. Prior to its complete landfall, Nari's circulation in the outer region is distributed by the higher-θ_e (>362 K) air in the MBL from the northeast to southwest quadrants and the lower-θ_e (<352 K) air to the east of the CMR ridge, whereas its inner core region is generally filled by the MBL higher-θ_e air (with the highest-θ_e greater than 374 K) in the eye (Figure 12a). Note that the eye wall at this time, characterized with large θ_e gradients, is located near the inner edge of more intense radar echoes. After landfall, the lower-θ_e air on the CMR's lee side, which is of elevated origin, is being advected into Nari's eye by cyclonically converging flows, while most of the original higher-θ_e air in the eye is elevated through the Ekman pumping (see Figure 7). It is *this intrusion of the lower-θ_e air* that results in the breakdown of the higher-θ_e material surfaces in the eye wall, as also indicated by the split of concentrated radar echoes even in the northern coastal region (Figure 12b).

[28] At t = 30 h, the higher-θ_e air in the MBL continues to feed the western half TC vortex to produce deep convection and rainfall, whereas the eastern half TC vortex is dominated by the elevated lower-θ_e (<350 K) air, some of which is cyclonically advected into the inner core region such that the eastern portion of the eye wall becomes dissolved with sporadic rainfall (compare Figures 12c and 10a).

[29] When the CMR is totally removed, the storm is surrounded by high-θ_e air with little gradients in the MBL. In particular, the lower-θ_e air to the east in the full-terrain run is completely absent (compare Figures 12a and 12d). The thermodynamic properties after landfall generally remain similar to those prior to landfall, except for the diminishing high-θ_e air in the eye (compare Figures 12d–12f and 7). Note the markedly different thermal and kinematic structures 8 h after landfall between the two runs (compare Figures 12c and 12f). In addition, the storm produces weaker radar echo or rainfall over the western eye wall than that in the control run, despite the presence of the high-θ_e air in the MBL. As mentioned earlier, this could be attributed to the lack of CMR topographical lifting.

[30] To trace the origins of lower level air near the eye, the backward (t = 30–25 h) trajectories of air parcels A–F starting at the low level (σ = 0.94) are calculated and shown in Figure 13a. Two major origins of air parcels are evident: one from the north and the east (trajectories A, B, C, and E) with high-θ_e origins (>359 K) and the other from the southeast (trajectories D and F) with low-θ_e origins (<349 K). The intrusion of the low-θ_e air from the southeast (on the eastern lee side of the CMR) is better shown in Figure 13b, which clearly indicates that the low-θ_e air mixes and replaces the original high-θ_e air inside the eye, and then dissolve the eye wall structure.

6. Summary and Conclusions

[31] In this paper, we analyzed a series of the cloud-resolving simulations of Typhoon Nari (2001) with and without the inclusion of Taiwan topography, as presented by *Yang et al.* [2008], in order to gain insight into the landfall characteristics of TCs over Taiwan. Three (oceanic, partial and complete landfall) stages of the storm evolution are selected to characterize the structural changes, especially terrain-induced asymmetries, of precipitation and kinematic fields during the landfall period.

[32] Results show that after landfall, the tangential flow is weakened but the low-level inflow and radial outflow immediately above the terrain are strengthened, due to the increased terrain blocking and surface friction. The eye wall updrafts exhibit more cellular structures with little influence from the large-scale vertical wind shear. Meanwhile, the radial outflow in the eye wall tilts more outward, and transports more hydrometeors generated in the inner region to outer rainbands, thereby broadening the surface precipitation area. The slantwise radial outflow is almost absent and the eye wall updrafts are mainly determined by the large-scale vertical shear when the terrain is removed, indicating that *the midlevel radial outflows and updrafts are the dynamic response of Nari's tangential circulation to the CMR*. At the time of landfall, Nari exhibits stronger primary and secondary circulations in the presence of the CMR

Figure 13. (a) Air parcel backward (30–25 h) trajectories with hourly positions indicated by arrows with hourly values of height (in m) and equivalent potential temperature (θ_e; in K). Blue shading is near-surface radar reflectivity at t = 30 h. Horizontal position of vertical cross sections in Figure 10 is indicated by the thin line. Terrain height of 1000 m is indicated by the thick gray line. (b) Zoom of backward trajectories superimposed with near-surface (σ = 0.94) colored θ_e field at t = 30 h. The θ_e contours of 350 and 352 K are added. Terrain height at 500 m interval is included.

topography than those without the topography, due to the enhanced latent heat release associated with heavy rainfall on the windward side of the CMR.

[33] It is found that radii of the near-surface maximum wind and the midlevel eye wall updraft could continue to contract even after landfall due to the continued rapid release of latent heat, but more pronounced in the western portion where Nari's vortex is subject to more topographical retardation and lifting. However, at later stages when the latent heating rates decrease, the inner core vortex size begins to increase and the storm weakens slowly.

[34] It is shown that because of its high elevation, the CMR allows Nari's vortex circulation to access the midlevel lower-θ_e air, as determined by backward trajectory analysis. Its intrusion into the inner core region causes the breakdown of the eye wall and dilution of the higher-θ_e air in the eye's boundary layer. The eye wall breakdown is also shown from the generation of concentrated PV in the eye wall on the windward side where intense latent heating occurs and of radially outward decreased PV on the lee side where little latent heating occurs. Based on the above results, we may conclude that the interaction of Nari's vortex circulation with the elevated lower-θ_e air, combined with the CMR topographical lifting and suppression effects, accounts for most of the asymmetrical structures after landfall.

[35] It should be mentioned that the above conclusions are obtained from the cloud-resolving control and sensitivity simulations of a single tropical cyclone case on Taiwan in which some model deficiencies still exist. More cases for landfall tropical cyclones over steep terrain are required in the future in order to generalize the results found in this study.

[36] **Acknowledgments.** This work was supported by the National Science Council of Taiwan under grants NSC 97-2111-M-008-019-MY3, NSC 97-2625-M-008-014, and NSC 98-2625-M-008-002. D.L.Z. was also supported by the U.S. National Science Foundation grant ATM-0758609, and Office of Navy Research grant N000140710186 and by the Typhoon Research Project (2009CB421503) of the National Basic Research Program (the 973 Program) of China. X.D.T. was supported by the National Natural Science Foundation of China under grant 40705018. Y.Z. was supported by the National Natural Science Foundation of China under grant 40605017 and the National Special Funding Project for Meteorology (GYHY201006004).

References

Bender, M. A., R. E. Tuleya, and Y. Kurihara (1987), A numerical study of the effect of island terrain on tropical cyclones, *Mon. Weather Rev.*, *115*, 130–155, doi:10.1175/1520-0493(1987)115<0130:ANSOTE>2.0.CO;2.

Black, M. L., J. F. Gamache, F. D. Marks, C. E. Samsury, and H. E. Willoughby (2002), Eastern Pacific hurricanes Jimena and Olivia of 1994: The effect of vertical shear on structure and intensity, *Mon. Weather Rev.*, *130*, 2291–2312, doi:10.1175/1520-0493(2002)130<2291:EPHJOA>2.0.CO;2.

Braun, S. A. (2006), High-resolution simulation of Hurricane Bonnie (1998). Part II: Water budget, *J. Atmos. Sci.*, *63*, 43–64, doi:10.1175/JAS3609.1.

Chen, Y., and M. K. Yau (2003), Asymmetric structures in a simulated landfalling hurricane, *J. Atmos. Sci.*, *60*, 2294–2312, doi:10.1175/1520-0469(2003)060<2294:ASIASL>2.0.CO;2.

Emanuel, K. A. (1997), Some aspects of hurricane inner-core dynamics and energetics, *J. Atmos. Sci.*, *54*, 1014–1026, doi:10.1175/1520-0469(1997)054<1014:SAOHIC>2.0.CO;2.

Guinn, T. A., and W. H. Schubert (1993), Hurricane spiral bands, *J. Atmos. Sci.*, *50*, 3380–3403, doi:10.1175/1520-0469(1993)050<3380:HSB>2.0.CO;2.

Houze, R. A., Jr., S. S. Chen, W.-C. Lee, R. Rogers, J. Moore, G. Stossmeister, M. Bell, J. Cetrone, W. Zhao, and S. Brodzik (2006), The Hurricane Rainband and Intensity Change Experiment: Observations and modeling of hurricanes Katrina, Ophelia, and Rita, *Bull. Am. Meteorol. Soc.*, *87*, 1503–1521, doi:10.1175/BAMS-87-11-1503.

Jorgensen, D. P. (1984a), Mesoscale and convective-scale characteristics of mature hurricanes. Part I: General observations by research aircraft, *J. Atmos. Sci.*, *41*, 1268–1286, doi:10.1175/1520-0469(1984)041<1268:MACSCO>2.0.CO;2.

Jorgensen, D. P. (1984b), Mesoscale and convective-scale characteristics of mature hurricanes. Part II: Inner core structure of Hurricane Allen (1980), *J. Atmos. Sci.*, *41*, 1287–1311, doi:10.1175/1520-0469(1984)041<1287:MACSCO>2.0.CO;2.

Lee, C.-S., Y.-C. Liu, and F.-C. Chien (2008), The secondary low and heavy rainfall associated with Typhoon Mindulle (2004), *Mon. Weather Rev.*, *136*, 1260–1283, doi:10.1175/2007MWR2069.1.

Lin, Y.-L., D. W. Hamilton, and C.-Y. Huang (1999), Orographic influence on drifting cyclones, *J. Atmos. Sci.*, *56*, 534–562, doi:10.1175/1520-0469(1999)056<0534:OIOADC>2.0.CO;2.

Lin, Y. L., D. B. Ensley, S. Chiao, and C.-Y. Huang (2002), Orographic influences on rainfall and track deflection associated with the passage of a tropical cyclone, *Mon. Weather Rev.*, *130*, 2929–2950, doi:10.1175/1520-0493(2002)130<2929:OIORAT>2.0.CO;2.

Liu, Y., D.-L. Zhang, and M. K. Yau (1999), A multiscale numerical study of hurricane Andrew (1992). Part II: Kinematics and inner-core structures, *Mon. Weather Rev.*, *127*, 2597–2616, doi:10.1175/1520-0493(1999)127<2597:AMNSOH>2.0.CO;2.

Marks, F. D., Jr., and R. A. Houze Jr. (1987), Inner core structure of Hurricane Alicia from airborne Doppler radar observations, *J. Atmos. Sci.*, *44*, 1296–1317, doi:10.1175/1520-0469(1987)044<1296:ICSOHA>2.0.CO;2.

Marks, F. D., Jr., R. A. Houze Jr., and J. F. Gamache (1992), Dual-aircraft investigation of the inner core of Hurricane Norbert. Part I: Kinematic structure, *J. Atmos. Sci.*, *49*, 919–942, doi:10.1175/1520-0469(1992)049<0919:DAIOTI>2.0.CO;2.

Reisner, J., R. J. Rasmussen, and R. T. Bruitjes (1998), Explicit forecasting of supercooled liquid water in winter storms using the MM5 mesoscaled model, *Q. J. R. Meteorol. Soc.*, *124*, 1071–1107, doi:10.1002/qj.49712454804.

Riehl, H. (1948), A radiosonde observation in the eye of a hurricane, *Q. J. R. Meteorol. Soc.*, *74*, 194–196, doi:10.1002/qj.49707432011.

Riehl, H. (1954), *Tropical Meteorology*, 392 pp., McGraw-Hill, New York.

Roux, F., and N. Viltard (1995), Structure and evolution of Hurricane Claudette on 7 September 1991 from airborne Doppler radar observation. Part I: Kinematics, *Mon. Weather Rev.*, *123*, 2611–2639, doi:10.1175/1520-0493(1995)123<2611:SAEOHC>2.0.CO;2.

Schubert, W. H., and J. J. Hack (1982), Inertial stability and tropical cyclone development, *J. Atmos. Sci.*, *39*, 1687–1697, doi:10.1175/1520-0469(1982)039<1687:ISATCD>2.0.CO;2.

Shapiro, L. J., and H. E. Willoughby (1982), The response of balanced hurricanes to local sources of heat and momentum, *J. Atmos. Sci.*, *39*, 378–394, doi:10.1175/1520-0469(1982)039<0378:TROBHT>2.0.CO;2.

Shea, D. J., and W. M. Gray (1973), The hurricane's inner core region. I. Symmetric and asymmetric structure, *J. Atmos. Sci.*, *30*, 1544–1564, doi:10.1175/1520-0469(1973)030<1544:THICRI>2.0.CO;2.

Simpson, R. H. (1952), Exploring the eye of Typhoon "Marge," 1951, *Bull. Am. Meteorol. Soc.*, *33*, 286–298.

Smith, R. K. (1980), Tropical cyclone eye dynamics, *J. Atmos. Sci.*, *37*, 1227–1232, doi:10.1175/1520-0469(1980)037<1227:TCED>2.0.CO;2.

Stear, J. R. (1965), Sounding in the eye of Hurricane Aelene to 108760 feet, *Mon. Weather Rev.*, *93*, 380–382, doi:10.1175/1520-0493(1993)093<0380:SITEOH>2.3.CO;2.

Tuleya, R. E. (1994), Tropical storm development and decay: Sensitivity to surface boundary conditions, *Mon. Weather Rev.*, *122*, 291–304, doi:10.1175/1520-0493(1994)122<0291:TSDADS>2.0.CO;2.

Willoughby, H. E. (1979), Forced secondary circulations in hurricanes, *J. Geophys. Res.*, *84*, 3173–3183, doi:10.1029/JC084iC06p03173.

Willoughby, H. E., and P. G. Black (1996), Hurricane Andrew in Florida: Dynamics of a disaster, *Bull. Am. Meteorol. Soc.*, *77*, 543–549, doi:10.1175/1520-0477(1996)077<0543:HAIFDO>2.0.CO;2.

Willoughby, H. E., J. A. Clos, and M. G. Shoreibah (1982), Concentric eye walls, secondary wind maxima, and the evolution of the hurricane vortex, *J. Atmos. Sci.*, *39*, 395–411, doi:10.1175/1520-0469(1982)039<0395:CEWSWM>2.0.CO;2.

Wu, C.-C., T.-H. Yen, Y.-H. Kuo, and W. Wang (2002), Rainfall simulation associated with Typhoon Herb (1996) near Taiwan. Part I: The topographic effect, *Weather Forecast.*, *17*, 1001–1015, doi:10.1175/1520-0434(2003)017<1001:RSAWTH>2.0.CO;2.

Yang, M.-J., and L. Ching (2005), A modeling study of Typhoon Toraji (2001): Physical parameterization sensitivity and topographic effect, *Terr. Atmos. Oceanic Sci.*, *16*, 177–213.

Yang, M.-J., D.-L. Zhang, and H.-L. Huang (2008), A modeling study of Typhoon Nari (2001) at landfall. Part I: Topographic effects, *J. Atmos. Sci.*, *65*, 3095–3115, doi:10.1175/2008JAS2453.1.

Yau, M. K., Y. Liu, D.-L. Zhang, and Y. Chen (2004), A multiscale numerical study of Hurricane Andrew (1992). Part VI: Small-scale inner-core structures and wind streaks, *Mon. Weather Rev.*, *132*, 1410–1433, doi:10.1175/1520-0493(2004)132<1410:AMNSOH>2.0.CO;2.

Yeh, T.-C., and R. L. Elsberry (1993a), Interaction of typhoons with the Taiwan orography. Part I: Upstream track deflections, *Mon. Weather Rev.*, *121*, 3193–3212, doi:10.1175/1520-0493(1993)121<3193:IOTWTT>2.0.CO;2.

Yeh, T.-C., and R. L. Elsberry (1993b), Interaction of typhoons with the Taiwan orography. Part II: Continuous and discontinuous tracks across the island, *Mon. Weather Rev.*, *121*, 3213–3233, doi:10.1175/1520-0493(1993)121<3213:IOTWTT>2.0.CO;2.

Zhang, D.-L., and C. Q. Kieu (2006), Potential vorticity diagnosis of a simulated hurricane. Part II: Quasi-balanced contributions to forced secondary circulations, *J. Atmos. Sci.*, *63*, 2898–2914, doi:10.1175/JAS3790.1.

Zhang, D.-L., Y. Liu, and M. K. Yau (2000), A multiscale numerical study of Hurricane Andrew (1992). Part III: Dynamically induced vertical motion, *Mon. Weather Rev.*, *128*, 3772–3788, doi:10.1175/1520-0493(2001)129<3772:AMNSOH>2.0.CO;2.

Zhu, T., D.-L. Zhang, and F. Weng (2004), Numerical simulation of Hurricane Bonnie (1998). Part I: Eyewall evolution and intensity changes, *Mon. Weather Rev.*, *132*, 225–241, doi:10.1175/1520-0493(2004)132<0225:NSOHBP>2.0.CO;2.

D.-L. Zhang, Department of Atmospheric and Oceanic Science, University of Maryland, 3419 CSS Bldg., College Park, MD 20742-2425, USA.

X.-D. Tang and Y. Zhang, Key Laboratory of Mesoscale Severe Weather, Ministry of Education, School of Atmospheric Sciences, Nanjing University, 22 Hankou Road, Nanjing Jiangsu 210093, China.

M.-J. Yang, Department of Atmospheric Sciences, National Central University, 300 Chung-Da Road Chung-Li, 320, Taiwan. (mingjen@ncu.edu.tw)